Controlling electron quantum paths for generation of circularly polarized high-order harmonics by H_{2}^{+} subject to tailored (ω, 2ω) counter-rotating laser fields

John Heslar, Dmitry A. Telnov, and Shih-I Chu

Controlling electron quantum paths for generation of circularly polarized high-order harmonics by H_2^+ subject to tailored $(\omega, 2\omega)$ counter-rotating laser fields

John Heslar,[1, *] Dmitry A. Telnov,[2, †] and Shih-I Chu[1, 3, ‡]

[1]*Department of Physics, Center for Quantum Science and Engineering,*
Center for Advanced Study in Theoretical Sciences,
National Taiwan University, Taipei 10617, Taiwan
[2]*Department of Physics, St. Petersburg State University,*
7-9 Universitetskaya naberezhnaya, St. Petersburg 199034, Russia
[3]*Department of Chemistry, University of Kansas, Lawrence, Kansas 66045, USA*

Recently, studies of high-order harmonics (HHG) from atoms driven by bichromatic counter-rotating circularly polarized laser fields as a source of coherent circularly polarized extreme ultra-violet (XUV) and soft x-ray beams in a tabletop-scale setup have received considerable attention. Here, we demonstrate the ability to control the electron recollisions giving three returns per one cycle of the fundamental frequency ω using tailored bichromatic $(\omega, 2\omega)$ counter-rotating circularly polarized laser fields with a molecular target. The full control of the electronic pathway is first analyzed by a classical trajectory analysis and then extended to a detailed quantum study of H_2^+ molecules in bichromatic $(\omega, 2\omega)$ counter-rotating circularly polarized laser fields. The radiation spectrum contains doublets of left and right circularly polarized harmonics in the XUV ranges. We study in detail the below-, near-, and above-threshold harmonic regions and describe how excited-state resonances alter the ellipticity and phase of the generated harmonic peaks.

I. INTRODUCTION

High-order-harmonic generation (HHG) is an attractive table-top source of coherent, bright, and tunable extreme ultraviolet (XUV) and soft X-ray radiation with applications in coherent diffractive imaging, ultrafast holography, and time resolved measurements [1–6]. Moreover, circularly polarized HHG may find additional applications in nanolithography, ultrafast spin dynamics, and magnetic circular dichroism [1, 7–13].

A direct approach for generating circularly polarized HHG was suggested 22 years ago [14, 15], and recently measured by Fleischer *et al.* [7]. In this scheme, circularly polarized HHG are driven by co-propagating circularly polarized bichromatic fields that rotate in opposite directions (counter-rotating) and interact with argon gas. This experiment [7] opened up the possibility and motivation of generating bright circularly polarized HHG comparable to the flux efficiency of linearly polarized HHG. Recently, Fan *et al.* [1] did just that, they generated bright circularly polarized soft X-ray HHG beams with photon energies greater than 160 eV and flux comparable to the HHG flux obtained using linearly polarized 800 nm driving lasers. These bright circularly polarized high-order-harmonic beams in the soft X-ray region were generated from He, Ne, and Ar atoms, and used to implement X-ray magnetic circular dichroism measurements in a tabletop-scale setup [1]. Previously, such radiation has only been available at large-scale X-ray facilities such as synchrotrons.

The primary characteristics of the bichromatic circularly polarized HHG spectra can be described in terms of the energy and angular momentum conservation, which gives rise to a doublet structure of the HHG spectrum. The right peak in the doublet has a circular polarization with the same helicity as the driving field with the higher frequency, the left peak has a circular polarization with the same helicity as the driving field with the lower frequency [1, 7–13, 16, 17]. The driving laser field parameters determine the spectral, temporal, and polarization properties of the circularly polarized HHG, enabling the creation of tailored circularly polarized HHG waveforms [16]. For instance, the frequencies of the bichromatic laser field can be chosen to tune the photon energy and bandwidth of the emitted harmonics from the XUV to the soft x-ray region [1, 16]. Also, in the same respect the relative intensity ratio of the bichromatic laser field can be adjusted to preferentially select either the right or left circularly polarized harmonics [16]. In the frequency domain, this enhances the harmonic orders that rotate in the same direction as the higher-intensity driving laser.

While an impressive progress has been achieved in generation of bright circularly polarized radiation by atomic targets, this area remains largely unexplored for molecular systems. In this work, we address the problem with the H_2^+ molecule subject to bichromatic counter-rotating circularly polarized intense laser fields and adopt wavelengths (790 nm and 395 nm) reported in a recent experiment [16]. We show through the use of a tailored relative intensity ratio of the bichromatic laser field we can generate radiation with circular polarization and have control over the electronic recollisions in the time domain for the H_2^+ molecule. We control the period of the recollisions with help from the classical trajectory analysis and apply it to a nonperturbative quantum investigation to produce a recollision event that features three

_____

* john.heslar@gmail.com
† d.telnov@spbu.ru
‡ sichu@ku.edu

returns for any 790 nm cycle during the laser pulse. We also find excited-state resonances can alter neighboring doublet structures in the HHG spectrum, and can also deviate the phase and ellipticity of neighboring doublets breaking down their perfect circular polarization.

The organization of this paper is as follows. In Sec. II we briefly discuss our theoretical and computational approach for the general treatment of the multiphoton dynamics of diatomic molecular systems subject to bichromatic counter-rotating circularly polarized intense laser fields. In Sec. III we explore the control of the electronic pathway with use of the standard classical approach. In Sec. IV we study HHG of H_2^+ molecules driven by bichromatic counter-rotating circularly polarized laser pulses. The HHG spectra exhibit a distinct doublet structure, and the harmonics within each doublet possess circular polarizations with opposite handedness. In Sec. V we employ the synchrosqueezing transform (SST) to analyze the time-frequency spectra of the below-, near-, and above-threshold HHG of H_2^+. We show that the electron returns are controlled with the intensity parameters used, and three dominant returns are seen within one cycle of the 790 nm field. In Sec. VI we provide a proof of perfect circular polarization and opposite handedness of the harmonics within the doublets, by calculating their ellipticity and phase parameters from the dipole acceleration data for below-, near-, and above-threshold HHG regions. We also show that excited-state resonances have effects on neighboring harmonics altering their perfect circular polarization. Section VII contains concluding remarks.

II. THEORY AND NUMERICAL TECHNIQUES

To calculate the HHG spectra, we solve the time-dependent Schrödinger equation for the H_2^+ molecule in the bichromatic counter-rotating circularly polarized laser fields. The initial wave function is an unperturbed eigenfunction of H_2^+. For our calculations, we select the ground ($1\sigma_g$) electronic state. The nuclei are fixed at their positions, and the nuclear motion is not taken into account. To describe the diatomic molecular ion H_2^+, we make use of the prolate spheroidal coordinates ξ, η, and φ which are related to the Cartesian coordinates x, y, and z as follows [18]:

$$
\begin{aligned}
x &= a\sqrt{(\xi^2-1)(1-\eta^2)}\cos\varphi, \\
y &= a\sqrt{(\xi^2-1)(1-\eta^2)}\sin\varphi, \\
z &= a\xi\eta \quad (1 \le \xi < \infty, -1 \le \eta \le 1).
\end{aligned}
\tag{1}
$$

In Eq. (1) we assume that the molecular axis is directed along the z axis, and the nuclei are located on this axis at the positions $-a$ and a, so the internuclear separation $R = 2a$. The internuclear distance for the H_2^+ ($R_e = 2.00a_0$) molecule is fixed at its equilibrium distance R_e.

A. Generalized pseudospectral method and solution of time-independent eigenvalue problem

First, we solve the unperturbed eigenvalue problem and obtain the eigenvalues and eigenfunctions:

$$
[-\frac{1}{2}\nabla^2 + U(\xi,\eta)]\Psi(\xi,\eta,\varphi) = E\Psi(\xi,\eta,\varphi).
\tag{2}
$$

Here the kinetic energy operator in the prolate spheroidal coordinates reads as:

$$
-\frac{1}{2}\nabla^2 = -\frac{1}{2a^2}\frac{1}{(\xi^2-\eta^2)}\left(\frac{\partial}{\partial\xi}(\xi^2-1)\frac{\partial}{\partial\xi} + \frac{\partial}{\partial\eta}(1-\eta^2)\frac{\partial}{\partial\eta} + \frac{\xi^2-\eta^2}{(\xi^2-1)(1-\eta^2)}\frac{\partial^2}{\partial\varphi^2}\right),
\tag{3}
$$

and the Coulomb interaction with the nuclei is as follows (the charge of each center is unity):

$$
U(\xi,\eta) = -\frac{2\xi}{a(\xi^2-\eta^2)}.
\tag{4}
$$

For the unperturbed molecule, the projection m of the angular momentum onto the molecular axis is conserved. Thus the wave function $\Psi(\xi,\eta,\varphi)$ can be represented in a separable form,

$$
\Psi(\xi,\eta,\varphi) = \psi_m(\xi,\eta)\exp(im\varphi),
\tag{5}
$$

and separate eigenvalues problems for different $|m|$ are obtained,

$$
-\frac{1}{2a^2}\frac{1}{(\xi^2-\eta^2)}\left[\frac{\partial}{\partial\xi}(\xi^2-1)\frac{\partial}{\partial\xi} + \frac{\partial}{\partial\eta}(1-\eta^2)\frac{\partial}{\partial\eta} - \frac{m^2}{\xi^2-1} - \frac{m^2}{1-\eta^2}\right]\psi_m = E\psi_m.
\tag{6}
$$

To solve Eq. (6), we use the generalized pseudospectral (GPS) method. Note that the *exact* eigenfunction ψ_m behaves as $(\xi^2-1)^{|m|/2}(1-\eta^2)^{|m|/2}$ in the vicinity of the nuclei; for odd $|m|$, this is a nonanalytical function of the coordinates. Straightforward numerical differentiation of such a function could result in signicant loss of accuracy. We circumvent this difficulty by choosing a special mapping transformation within the GPS method [19]. Other details of the GPS method in prolate spheroidal coordinates can be found in Refs. [20–24].

Solving the eigenvalue problem (6) for different even and odd m, we obtain unperturbed energy values and eigenstates of H_2^+, which are used as initial states for time propagation as well as for construction of propagation matrices.

B. Solution of the time-dependent Schrödinger equation in bichromatic circularly polarized laser pulses

The time-dependent Schrödinger equation in the bichromatic circularly polarized laser pulses is solved

by means of the split-operator method in the energy representation [20–25]. We employ the following split-operator, second-order short-time propagation formula:

$$\Psi(t + \Delta t) = \exp(-i\frac{1}{2}\Delta t H_0)$$
$$\times \exp[-i\Delta t V_{\text{ext}}(\boldsymbol{r}, t + \frac{1}{2}\Delta t)] \quad (7)$$
$$\times \exp(-i\frac{1}{2}\Delta t H_0) + O((\Delta t)^3).$$

Here Δt is the time propagation step, H_0 is the unperturbed electronic Hamiltonian which includes the kinetic energy and interaction with the nuclei, $V_{\text{ext}}(\boldsymbol{r}, t)$ is the term due to the coupling to the bichromatic circularly polarized external fields, in the following form:

$$V_{\text{ext}}(\boldsymbol{r}, t) = [\boldsymbol{E}_1(t) + \boldsymbol{E}_2(t)] \cdot \boldsymbol{r}. \quad (8)$$

The laser electric-field strengths $\boldsymbol{E}_1(t)$ and $\boldsymbol{E}_2(t)$ refer to the two frequency components of the bichromatic field.

In what follows, we shall assume that the laser fields $\boldsymbol{E}_1(t)$ and $\boldsymbol{E}_2(t)$ propagate along the z axis and have circular polarizations on the $x-y$ plane. The counter-rotating fields $\boldsymbol{E}_1(t)$ and $\boldsymbol{E}_2(t)$ are expressed as follows:

$$\boldsymbol{E}_1(t) = \frac{1}{\sqrt{2}}F_1(t)\left[\hat{\boldsymbol{e}}_x \cos(\omega_1 t) + \hat{\boldsymbol{e}}_y \sin(\omega_1 t)\right], \quad (9)$$

$$\boldsymbol{E}_2(t) = \frac{1}{\sqrt{2}}F_2(t)\left[\hat{\boldsymbol{e}}_x \cos(\omega_2 t) - \hat{\boldsymbol{e}}_y \sin(\omega_2 t)\right]. \quad (10)$$

Since the dipole approximation is well justified in the near infrared and visible wavelength region, the fields are assumed uniform in space. In Eqs. (9) and (10), ω_1 and ω_2 denote the carrier frequencies while $F_1(t)$ and $F_2(t)$ represent the temporal pulse envelopes. We use the sine-squared pulse shape:

$$F_1(t) = F_1 \sin^2 \frac{\pi t}{N_1 T_1}, \quad (11)$$

$$F_2(t) = F_2 \sin^2 \frac{\pi t}{N_2 T_2}, \quad (12)$$

where F_1 and F_2 are the peak electric field strengths, T_1 and T_2 are the optical cycle durations for each field [$T_1 = 2\pi/\omega_1$ and $T_2 = 2\pi/\omega_2$], and the integer numbers N_1 and N_2 are the total pulse durations measured in optical cycles.

The dipole interaction potentials in the length gauge have the following expressions in the prolate spheroidal coordinates:

$$\boldsymbol{E}_1(t) \cdot \boldsymbol{r} = \frac{a}{\sqrt{2}}F_1(t)\sqrt{(\xi^2 - 1)(1 - \eta^2)} \quad (13)$$
$$\times \cos(\varphi - \omega_1 t),$$

$$\boldsymbol{E}_2(t) \cdot \boldsymbol{r} = \frac{a}{\sqrt{2}}F_2(t)\sqrt{(\xi^2 - 1)(1 - \eta^2)} \quad (14)$$
$$\times \cos(\varphi + \omega_2 t).$$

In our calculations, we use the carrier wavelengths 395 nm for the field $\boldsymbol{E}_1(t)$ ($\omega_1 = 0.1153$ a.u.$= 3.14$ eV) and 790 nm for the field $\boldsymbol{E}_2(t)$ ($\omega_2 = 0.0576$ a.u.$= 1.57$ eV), respectively. One cycle of the ω_1 and ω_2 fields are 1.32 and 2.64 fs, respectively. The peak field strengths F_1 and F_2 correspond to the intensities $I_1 = 2 \times 10^{14}$ W/cm^2 and $I_2 = 1.25 \times 10^{13}$ W/cm^2, respectively. The pulse durations are chosen as $N_1 = 34$ and $N_2 = 17$. The total pulse duration for both fields is 45 fs. To obtain converged HHG spectra for the laser field parameters used in the calculations, we set the grid size (for ξ, η, and φ coordinates, respectively) to $160 \times 48 \times 48$ and use 4096 time steps per one 395 nm (ω_1) optical cycle in the time propagation process. The spatial and temporal grid parameters have been varied to make sure all the results are fully converged. The linear dimension of the box where the time-dependent equations are solved is chosen as 50 a.u. to ensure accurate description of all important physics for the laser field parameters used in the calculations; between 30 and 50 a.u. we apply an absorber which smoothly brings down the propagated wave functions without spurious reflections from the boundary.

The HHG power spectra can be investigated accurately once the time-dependent wave function $\Psi(\xi, \eta, \varphi, t)$ is available. We calculate the expectation values of the induced dipole acceleration in the x, y, and z directions:

$$a_x(t) = \langle\Psi(\xi, \eta, \varphi, t)|\frac{\partial U(\xi, \eta)}{\partial x}|\Psi(\xi, \eta, \varphi, t)\rangle$$
$$+ E_{1x}(t) + E_{2x}(t), \quad (15)$$

$$a_y(t) = \langle\Psi(\xi, \eta, \varphi, t)|\frac{\partial U(\xi, \eta)}{\partial y}|\Psi(\xi, \eta, \varphi, t)\rangle$$
$$+ E_{1y}(t) + E_{2y}(t), \quad (16)$$

$$a_z(t) = \langle\Psi(\xi, \eta, \varphi, t)|\frac{\partial U(\xi, \eta)}{\partial z}|\Psi(\xi, \eta, \varphi, t)\rangle. \quad (17)$$

Then the power spectrum $S(\omega)$ (spectral density of the radiation energy) can be obtained by the Fourier transformation of the time-dependent dipole accelerations,

$$S_x(\omega) = \frac{2}{3\pi c^3}\left|\int_{-\infty}^{\infty} a_x(t)\exp(i\omega t)dt\right|^2, \quad (18)$$

$$S_y(\omega) = \frac{2}{3\pi c^3}\left|\int_{-\infty}^{\infty} a_y(t)\exp(i\omega t)dt\right|^2, \quad (19)$$

$$S_z(\omega) = \frac{2}{3\pi c^3}\left|\int_{-\infty}^{\infty} a_z(t)\exp(i\omega t)dt\right|^2, \quad (20)$$

$$S_{\text{tot}}(\omega) = S_x(\omega) + S_y(\omega) + S_z(\omega). \quad (21)$$

We note that for the homonuclear diatomic molecule H$_2^+$ initially in the state with the definite parity and laser fields polarized in the plane perpendicular to the molecular (z) axis, the contribution $S_z(\omega)$ vanishes.

III. CONTROLLING CLASSICAL RETURN TIMES FOR MOLECULES IN BICHROMATIC COUNTER-ROTATING CIRCULARLY POLARIZED LASER FIELDS

The classical trajectory of the electron subject to bichromatic counter-rotating circularly polarized laser fields in the $x-y$ plane is given by the equations:

$$
\begin{aligned}
x = & \frac{1}{\sqrt{2}} \left[\frac{F_1}{\omega_1^2} \cos \omega_1 t + \frac{F_2}{\omega_2^2} \cos \omega_2 t \right] \\
& + \frac{1}{\sqrt{2}} \left[\frac{F_1}{\omega_1} \sin \omega_1 t_0 + \frac{F_2}{\omega_2} \sin \omega_2 t_0 \right] (t - t_0) \\
& - \frac{1}{\sqrt{2}} \left[\frac{F_1}{\omega_1^2} \cos \omega_1 t_0 + \frac{F_2}{\omega_2^2} \cos \omega_2 t_0 \right],
\end{aligned}
\tag{22}
$$

$$
\begin{aligned}
y = & \frac{1}{\sqrt{2}} \left[\frac{F_1}{\omega_1^2} \sin \omega_1 t - \frac{F_2}{\omega_2^2} \sin \omega_2 t \right] \\
& - \frac{1}{\sqrt{2}} \left[\frac{F_1}{\omega_1} \cos \omega_1 t_0 - \frac{F_2}{\omega_2} \cos \omega_2 t_0 \right] (t - t_0) \\
& - \frac{1}{\sqrt{2}} \left[\frac{F_1}{\omega_1^2} \sin \omega_1 t_0 - \frac{F_2}{\omega_2^2} \sin \omega_2 t_0 \right].
\end{aligned}
\tag{23}
$$

Here F_1 and F_2 are constants, so the pulse envelope is not taken into account. This approximation is reasonable in the vicinity of the envelope maximum where the HHG mostly takes place. Eqs. (22) and (23) correspond to the zero position and zero velocity at $t = t_0$ and generally describe an infinite motion of the electron. A closed periodic trajectory is obtained with the zero drift velocity. In this case one has instead of Eqs. (22) and (23):

$$
\begin{aligned}
x = & \frac{1}{\sqrt{2}} \frac{F_1}{\omega_1^2} \left[\cos \omega_1 t - \cos \omega_1 t_0 \right] \\
& + \frac{1}{\sqrt{2}} \frac{F_2}{\omega_2^2} \left[\cos \omega_2 t - \cos \omega_2 t_0 \right],
\end{aligned}
\tag{24}
$$

$$
\begin{aligned}
y = & \frac{1}{\sqrt{2}} \frac{F_1}{\omega_1^2} \left[\sin \omega_1 t - \sin \omega_1 t_0 \right] \\
& - \frac{1}{\sqrt{2}} \frac{F_2}{\omega_2^2} \left[\sin \omega_2 t - \sin \omega_2 t_0 \right].
\end{aligned}
\tag{25}
$$

The period of this trajectory is equal to the largest of the two optical cycles (T_2), thus in the general case it returns to the origin once per every T_2 time interval. However, if the field strengths F_1 and F_2 satisfy the condition

$$
\frac{F_2}{F_1} = \frac{\omega_2^2}{\omega_1^2},
\tag{26}
$$

the trajectory may manifest three returns per T_2 optical cycle (2.64 fs) if a specific release time t_0 is chosen. The analytic expression of this trajectory for constant F_1 and F_2 is as follows ($\omega_2 t_0 = \pm \pi/3$):

$$
x = \frac{F_1 \sqrt{2}}{\omega_1^2} \cos \left(\frac{1}{2} \omega_2 t \right) \cos \left(\frac{3}{2} \omega_2 t \right),
\tag{27}
$$

$$
y = \frac{F_1 \sqrt{2}}{\omega_1^2} \sin \left(\frac{1}{2} \omega_2 t \right) \cos \left(\frac{3}{2} \omega_2 t \right).
\tag{28}
$$

This property (three returns per T_2 optical cycle) is also preserved for the pulse envelope functions defined in Eqs. (11) and (12). The distance from the origin in the $x-y$ plane is calculated as

$$
r = \sqrt{x^2 + y^2}.
\tag{29}
$$

A recollision event is detected when r approaches zero. Figure 1(a) shows $x(t)$, $y(t)$, and $r(t)$ for the envelope functions (11) and (12) and peak field strengths F_1 and F_2 corresponding to the intensities $I_1 = 2 \times 10^{14}$ W/cm² and $I_2 = 1.25 \times 10^{13}$ W/cm², respectively. The grey filled box shows three returns per T_2 optical cycle (2.64 fs) in the central part of the pulse (22.0–27.3 fs). In Fig. 1(b) we show the classical electron trajectory that features three returns (three fold rosette shape) for any T_2 cycle during the laser pulse.

The circularly polarized laser pulses in the x and y domain (E_x and E_y) using the controlled laser peak intensities I_1 and I_2 are shown in Figs. 2(a) and (b). Figure 2(a) shows the time-dependent electric field of the driving laser pulse for peak laser intensities of $I_1 = 2 \times 10^{14}$ W/cm² and $I_2 = 1.25 \times 10^{13}$ W/cm² for the total time duration of 45 fs. In Fig. 2(b) we show the counter-rotating laser fields in the $x-y$ polarization plane for the 45 fs time duration.

IV. CIRCULARLY POLARIZED HIGH-ORDER HARMONICS IN H_2^+ MOLECULES

The structure of the HHG spectra can be described in terms of the energy and angular momentum conservation in the process of absorption of the driving fields photons and emission of the harmonic photon [1, 6, 7, 13, 14, 16, 17, 26]. The energy conservation gives $\omega = n_1 \omega_1 + n_2 \omega_2$ for the frequency ω of the emitted photon after absorption of n_1 photons of frequency ω_1 and n_2 photons of frequency ω_2. The angular momentum conservation requires $n_2 = n_1 \pm 1$ or $n_2 = n_1$ for the circularly-polarized counter-rotating driving fields $\mathbf{E}_1$ and $\mathbf{E}_2$. However, for the quantum systems with inversion symmetry such as atoms and homonuclear diatomic molecules, emission of dipole radiation is forbidden in the case $n_2 = n_1$ due to parity restrictions. Then the emitted photon frequency can be represented as $\omega = (2n+1)(\omega_1+\omega_2)/2 \pm (\omega_1-\omega_2)/2$, n being a positive integer number. This gives rise to a doublet structure of the HHG spectrum, with the frequency differences $\omega_1+\omega_2$ between the adjacent doublets and $\omega_1 - \omega_2$ between the photon emission peaks within the same doublet. The right peak in the doublet has a circular polarization with the same helicity as the driving field with the higher frequency ($\mathbf{E}_1$), the left peak has a circular polarization
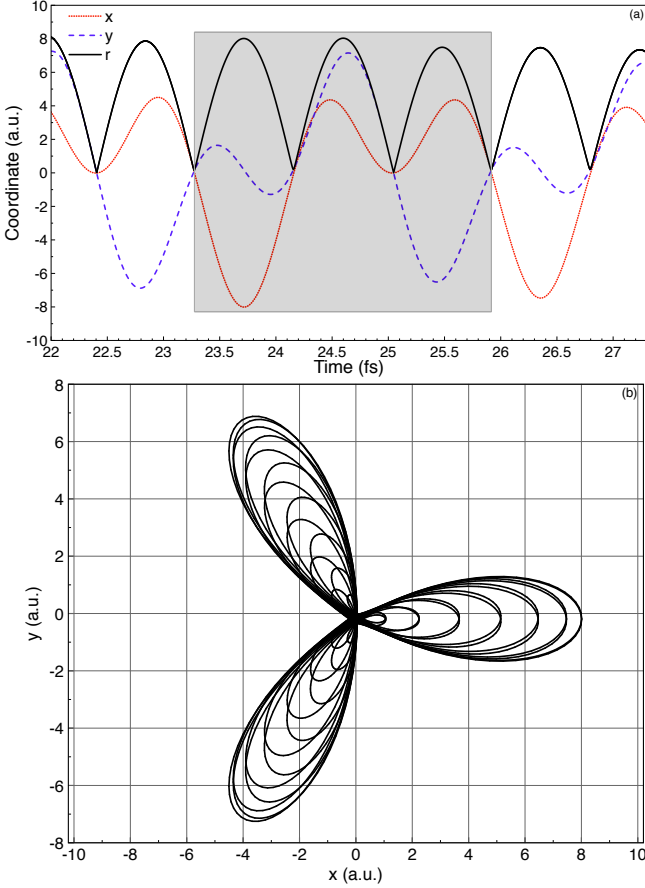
FIG. 1. (Color online) Classical trajectories for x, y, and r domains versus release time. (a) Scanning the release time t in the interval corresponding to the center of the pulse (22.0–27.3 fs). The grey filled box shows three returns per T_2 optical cycle (2.64 fs). (b) The trajectories of the three returns (three fold rosette shape) are shown for the total pulse duration (45 fs) in the x and y domain. The bichromatic frequency components have different peak field strengths corresponding to the intensities of $I_1 = 2 \times 10^{14}$ W/cm^2 and $I_2 = 1.25 \times 10^{13}$ W/cm^2.
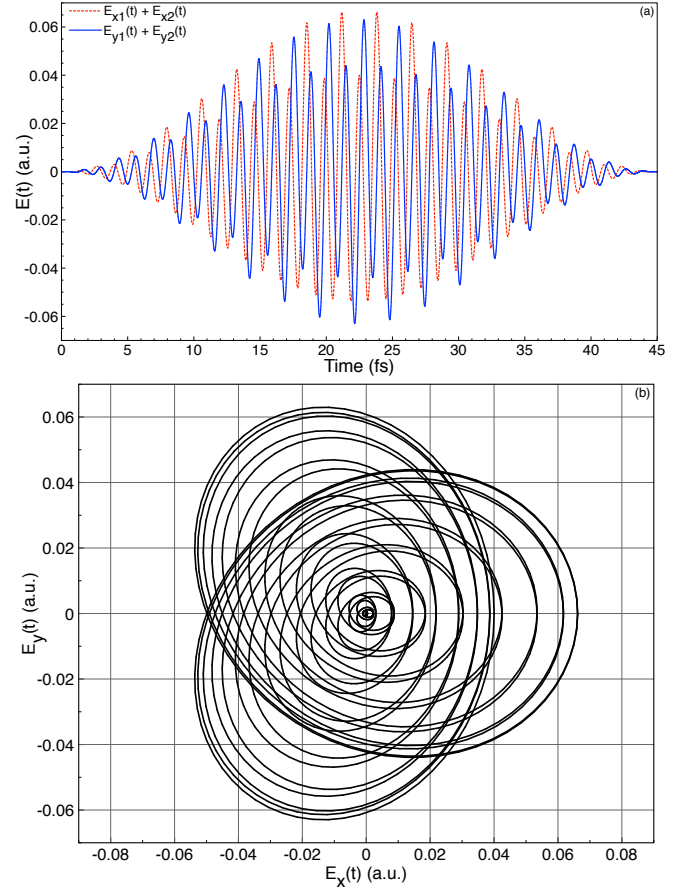

FIG. 2. (Color online) Time-dependent electric field of the driving laser pulse. (a) The red dotted and blue solid lines represent the electric field in the x and y direction, respectively. The laser pulse has a duration of 34 optical cycles (~ 45 fs) for the ω_1 (395 nm) component and 17 optical cycles (~ 45 fs) for the ω_2 (790 nm) component. The bichromatic frequency components have different peak field strengths corresponding to the intensities of $I_1 = 2 \times 10^{14}$ W/cm^2 and $I_2 = 1.25 \times 10^{13}$ W/cm^2. (b) The counter-rotating laser fields in the $x - y$ polarization plane for the total time duration of 45 fs.

with the same helicity as the driving field with the lower frequency ($\boldsymbol{E}_2$). If we define the ratio of the two frequencies $q = \omega_1/\omega_2$, we obtain $\omega = n(q + 1)\omega_2 \pm \omega_2$. In the case studied here, $q = 2$ and $\omega = (3n \pm 1)\omega_2$. The HHG spectrum consists of odd and even harmonics of the lowest frequency ω_2 except for the harmonic orders that are multiples of 3.

In Figs. 3 (a-d), we present the HHG spectrum of H$_2^+$ for the driving laser pulse shown in Fig. 2. The calculated HHG spectra for H$_2^+$ in Figs. 3 (a-d), respectively, show the peak positions match well those predicted by the selection rules and specified above. The spectrum displays circularly polarized harmonics up to the 81st harmonic order (H81). The ionization threshold (I_p) for the initially occupied $1\sigma_g$ molecular orbital is marked with the green dashed vertical line at $\sim$H19 (19.13ω_2).

Figure 3(b) shows the below- and near-threshold region (H1-H20). As one can see, the spectrum exhibits a clear doublet structure with the spacing between the main peaks equal to $3\omega_2$ and subpeak separation of ω_2. According to the general considerations discussed above, the components of the doublet (subpeaks within each main peak) must have circular polarizations opposite to each other. This rule is true except for higher order below-threshold harmonics (H10–H20). In this region, excitation of the bound states and subsequent near-resonant emission alters the shape of the neighboring doublets in the HHG spectrum. In Fig. 3(b) two resonant peaks (marked A and B) are comparable in their height with the nearby regular harmonic peaks. The resonances A and B correspond to the transitions $1\sigma_g - 1\pi_u$ (H11.7)

and $1\sigma_g - 2\pi_u$ (H15.6), respectively. Figures 3(c) and (d) show the above-threshold circularly polarized harmonics up to H74.

V. SST TIME-FREQUENCY SPECTRA

To analyze the underlying mechanism from the *ab initio* simulation, we perform the SST time-frequency analysis of the dipole acceleration for H_2^+ interacting with the applied laser fields. In previous studies [27], several representative time-frequency methods have been compared for the atomic hydrogen system including the short-time Fourier transforms, such as Gabor transform, Wigner-Ville transform [28] and the SST [29, 30], as well as the continuous wavelet transform, the bilinear time-frequency transform and the reallocation method, respectively. They found that both the Gabor and the Morlet transforms are subject to some obscure spectral features arising from a window and that the Wigner-Ville transform is accompanied by interference artifacts, resulting in incomprehensible analysis. Among these methods, only the SST can resolve the intrinsic blurring in the Gabor and the Morlet transforms [31]. Apart from the applications in atomic, molecular, and optical physics, the SST was successfully used for analysis of chronotaxic systems [32] and cardiovascular systems [33].

Here we perform the time-frequency SST analysis of the induced dipole accelerations $a_x(t)$, $a_y(t)$, and $a_z(t)$ in the H_2^+ diatomic molecule interacting with the applied laser fields [21, 27, 31, 34]. The synchrosqueezing transforms $\tilde{S}_x$, $\tilde{S}_y$, and $\tilde{S}_z$ of the corresponding dipole accelerations are defined as follows:

$$\tilde{S}_{x,y,z}(t,\tilde{\omega}) = \int \frac{1}{\sqrt{\omega}} V_{x,y,z}(t,\omega) \frac{1}{\alpha\sqrt{\pi}}$$
$$\times \exp\left(-\left[\frac{\tilde{\omega} - \Omega_{x,y,z}^f(t,\omega)}{\alpha}\right]^2\right) d\omega, \quad (30)$$

where $V_{x,y,z}(t,\omega)$ is the Morlet wavelet transform, $\Omega_{x,y,z}^f(t,\omega)$ is the reallocation rule function, and α is a smoothing parameter. In this study, $\alpha = 2.6$. The Morlet wavelet transform is given as:

$$V_{x,y,z}(t,\omega) = \int a_{x,y,z}(t')\sqrt{\omega} W(\omega(t'-t)) dt', \quad (31)$$

where

$$W(\beta) = \frac{1}{\sqrt{\tau}} \exp(i\beta) \exp\left(-\frac{\beta^2}{2\tau^2}\right), \quad (32)$$

is the mother wavelet. The reallocation rule function is defined as:

$$\Omega_{x,y,z}^f(t,\omega) = \begin{cases} \dfrac{-i\partial_t V_{x,y,z}(t,\omega)}{V_{x,y,z}(t,\omega)} & \text{for } V_{x,y,z}(t,\omega) \neq 0 \\ \infty & \text{for } V_{x,y,z}(t,\omega) = 0 \end{cases}, \quad (33)$$

where ∂_t denotes the partial derivative in the temporal axis. In Fig. 4 we show the total absolute value of the SST spectrum $|\tilde{S}_{\text{tot}}(t,\tilde{\omega})|$ calculated as:

$$|\tilde{S}_{\text{tot}}(t,\tilde{\omega})| = |\tilde{S}_x(t,\tilde{\omega})| + |\tilde{S}_y(t,\tilde{\omega})| + |\tilde{S}_z(t,\tilde{\omega})|. \quad (34)$$

The time-frequency spectrum $|\tilde{S}_{\text{tot}}|$ shows a periodic repetition of arches in the above-threshold region (>H19.13) spanning to the 65th harmonic order (H65). These periodic repetition of arches (>H19.13) are comprised of three returns per T_2 optical cycle (2.64 fs). The quantum SST time-frequency analysis shows the same phenomena (3 returns per T_2 optical cycle) as proposed by the controlled classical electron trajectories in Figs. 1(a) and (b).

VI. ELLIPTICITY AND RELATIVE PHASESHIFT OF HARMONIC RADIATION

According to the discussion in Sec. IV, generation of high-order harmonics by bichromatic counter-rotating circularly polarized laser fields results in harmonic doublets, where in each doublet the harmonics are circularly polarized with opposite handedness. However, this argument assumes that the driving field frequency components are perfectly monochromatic. In reality, the laser pulse has a finite duration, hence the harmonic peaks have a finite width, and polarization may vary even on the frequency range corresponding to the same harmonic peak. Near-resonant radiation from the excited states may also alter the polarization properties of the HHG spectrum in the below-threshold region. Here, we calculate the polarization properties of the harmonic radiation explicitly from the dipole acceleration data and show to what extent the harmonic peaks within the same doublet possess circular polarizations with left and right handedness.

Suppose we have a monochromatic field with the components along x and y:

$$\begin{aligned} F_x &= a\cos(\omega t), \\ F_y &= b\cos(\omega t + \beta). \end{aligned} \quad (35)$$

Generally, the field amplitudes along x and y are different (with their ratio $r_{yx} = b/a$), and there is a phaseshift β between the field oscillations in x and y directions. Actually, Eq. (35) represents an elliptically polarized field; the orientation of the ellipse in the $x - y$ plane depends on the parameters r_{yx} and β. The angle α which determines the orientation of one of the ellipse axes with respect to the x-axis is calculated as:

$$\alpha = -\frac{1}{2}\arctan\left(\frac{r_{yx}^2 \sin(2\beta)}{1 + r_{yx}^2 \cos(2\beta)}\right). \quad (36)$$

The second axis has the orientation angle $\alpha + \pi/2$. Assuming the first axis to be the major axis of the ellipse,
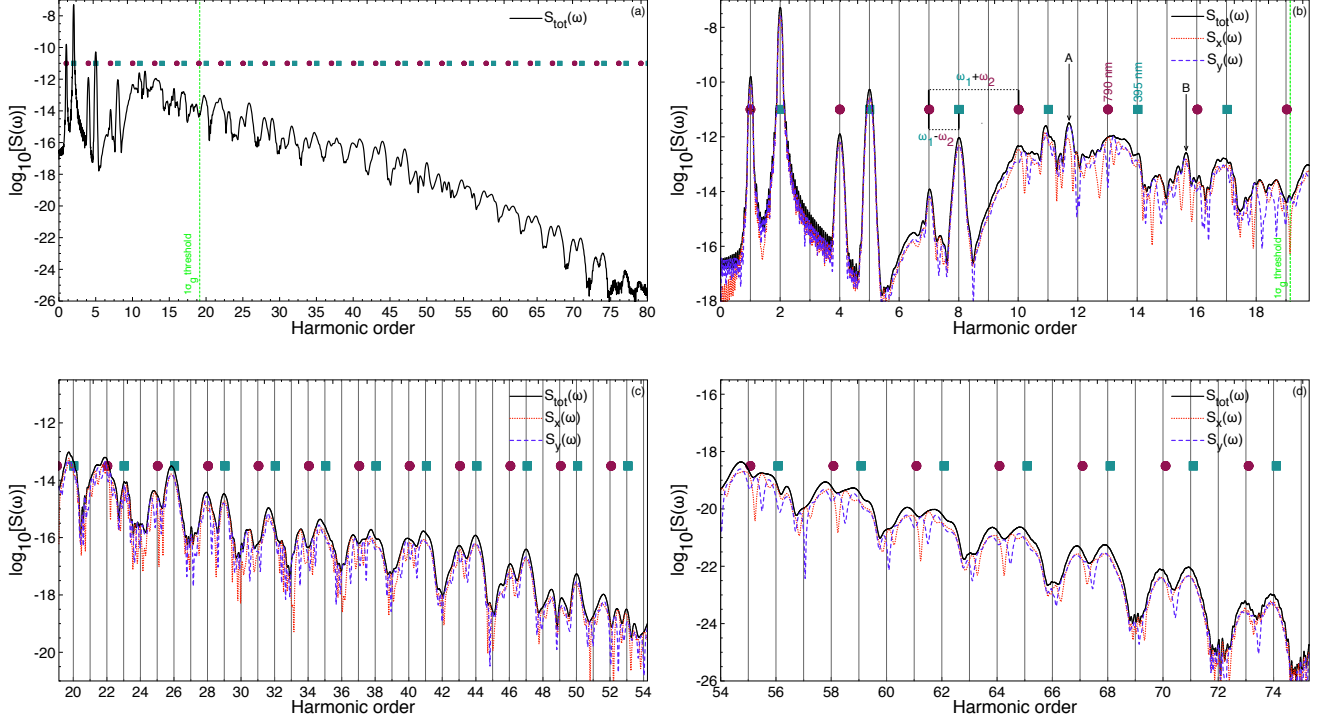
FIG. 3. (Color online) HHG spectrum $S(\omega)$ in the x, y, and total domain of the H_2^+ molecule in the counter-rotating circularly polarized laser pulses. Circularly polarized HHG spectrum (a) up to $\sim$H81, (b) below-threshold (H1-H20), (c) above-threshold; plateau region (H20-H53), and (d) above-threshold; plateau and near cutoff region (H55-H74). The laser pulses have a time duration of 34 optical cycles ($\sim$ 45 fs) for ω_1 (395 nm) and 17 optical cycles ($\sim$ 45 fs) for ω_2 (790 nm). The green vertical dashed line indicates the corresponding ionization threshold (I_p) marked by $1\sigma_g$ threshold (H19.13). Resonance A and B in panel (b) correspond to the transitions $1\sigma_g - 1\pi_u$ (H11.7) and $1\sigma_g - 2\pi_u$ (H15.6), respectively. All spectra show a doublet structure, located at positions predicted by energy and spin angular momentum conservation [filled maroon circles (790 nm) and filled teal squares (395 nm)]. The separation within each doublet is $\omega_1 - \omega_2 = \omega_2$, and different doublets are separated by $\omega_1 + \omega_2 = 3\omega_2$. The bichromatic frequency components have different peak field strengths corresponding to the intensities of $I_1 = 2 \times 10^{14}$ W/cm^2 and $I_2 = 1.25 \times 10^{13}$ W/cm^2.

the ellipticity parameter is calculated as follows:

$$\epsilon = \sqrt{\frac{\sin^2 \alpha + r_{yx}^2 \sin^2(\alpha + \beta)}{\cos^2 \alpha + r_{yx}^2 \cos^2(\alpha + \beta)}} \qquad (37)$$

If the calculated ellipticity parameter ϵ appears greater than unity, then the first axis is actually the minor axis, and the ellipticity parameter is given by $1/\epsilon$. From the Fourier transform of the induced dipole acceleration (which represents the harmonic field), one can obtain the parameters r_{yx} and β and calculate the ellipticity for the specific frequency ω. The circular polarization ($\epsilon = 1$) is only possible if $\beta = \pm\pi/2$ and $r_{yx} = 1$.

In Figs. 5-7, the filled maroon circles and filled teal squares indicate the positions of harmonic peaks within each doublet. The circular polarization of the harmonics marked with the teal squares has the same handedness (left-helicity) as that of the driving field $\boldsymbol{E}_1(t)$, and the harmonics marked with the maroon circles are polarized with the same handedness (right-helicity) as the driving field $\boldsymbol{E}_2(t)$.

Figure 5 shows the phase and ellipticity of the below-threshold harmonics in the HHG spectrum of the H_2^+ molecule (Fig 3). As one can see in Fig. 5, the ellipticity of the below-threshold harmonics is near unity and the phases are very close to $\pm\pi/2$, indicating circular polarizations with left and right handedness. The phase and ellipticity of the harmonics are altered in the region where the excited-state resonances start to appear, hence, $1\sigma_g - 1\pi_u$ (H11.7) and $1\sigma_g - 2\pi_u$ (H15.6) labeled by open blue oval marks in Figs. 5(a) and (b). The excited-state resonances have effects on neighboring harmonics causing the phase and ellipticity to alter from perfect circular polarization. In Fig. 3, the excited-state resonances altered the shape of the neighboring doublets (H10–H20) in the HHG spectra.

In the above-threshold plateau region (Figs. 6 and 7), the harmonics within the doublets still do not show perfect circular polarizations with their ellipticities and phases deviating from unity and $\pm\pi/2$, respectively. In the lower-energy part of this region (H19–H38, Fig. 6), right subpeaks in the doublets (teal squares) exhibit bet-
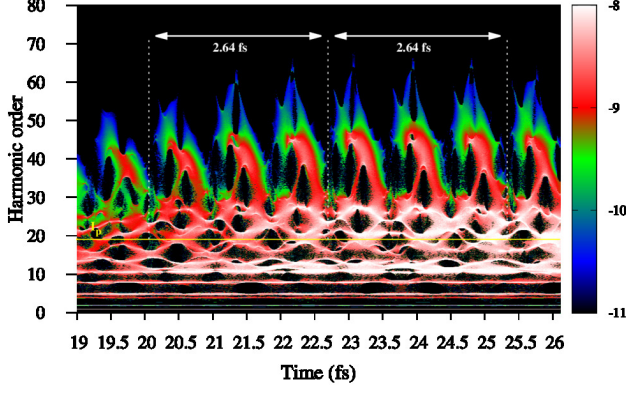
FIG. 4. (Color online) SST time-frequency analysis $|\tilde{S}_{\text{tot}}|$ of the HHG spectra of H_2^+. The horizontal yellow solid line indicates the ionization potential I_p at $\sim$H19. The vertical white dashed lines indicates one cycle (T_2) of the ω_2 field (2.64 fs). Three returns per T_2 optical cycle are observed, as proposed by the controlled classical electron trajectories in Figs. 1(a) and (b). The laser parameters used are the same as those in Fig. 3. The color scale is logarithmic.

FIG. 5. (Color online) (a) Ellipticity and (b) phaseshift between the x and y components of the harmonic field (below-threshold harmonics) from H_2^+ as a function of harmonic order. The laser parameters used are the same as those in Fig. 3. The filled maroon circles and filled teal squares mark the harmonic peak positions within each doublet. The open blue oval marks the $1\sigma_g - 1\pi_u$ (H11.7) and $1\sigma_g - 2\pi_u$ (H15.6) excited-state resonance peaks shown in Fig.3(b).

ter circular polarization than the left subpeaks (maroon circles). In the higher-energy part (H54–H65, Fig. 7), the pattern is reversed; here more perfect circular polarization is observed for the left subpeaks (maroon circles). Generally, perfect circular polarization can be expected when the harmonic signals polarized in the x and y directions have equal strengths. The x and y components of the harmonic radiation, in turn, are induced by the x and y components of the driving field. Averaged over the total pulse duration, the intensities of the x and y components of the driving field are the same, but they may differ significantly on shorter (subcycle) time intervals (see Fig. 2). Since the high-order harmonics are predominantly generated during short recollision events in the central part of the laser pulse, they may be affected by the asymmetry between the x and y components of the driving field. In our previous work [17], we showed that for small frequency difference $\omega_1 - \omega_2$ this asymmetry can lead to disappearance of the doublet structure and circular polarization of the harmonics in the HHG spectrum. In the present case $\omega_1 = 2\omega_2$, the doublet structure remains distinct but polarizations of the subpeaks may have significantly altered. As one can see from Fig. 3c, the x and y contributions to the harmonic signal are very close to each other for the right subpeaks (teal squares) while considerable difference between these contributions is observed for the left subpeaks (maroon circles). Consequently, perfect circular polarization cannot be expected for the left subpeaks, in accordance with the results presented in Fig. 6. The pattern is changed for the higher-order harmonics, H54–H65. In this part of the spectrum (Fig. 3d), the x and y contributions to the harmonic signal are closer to each other for the left subpeaks
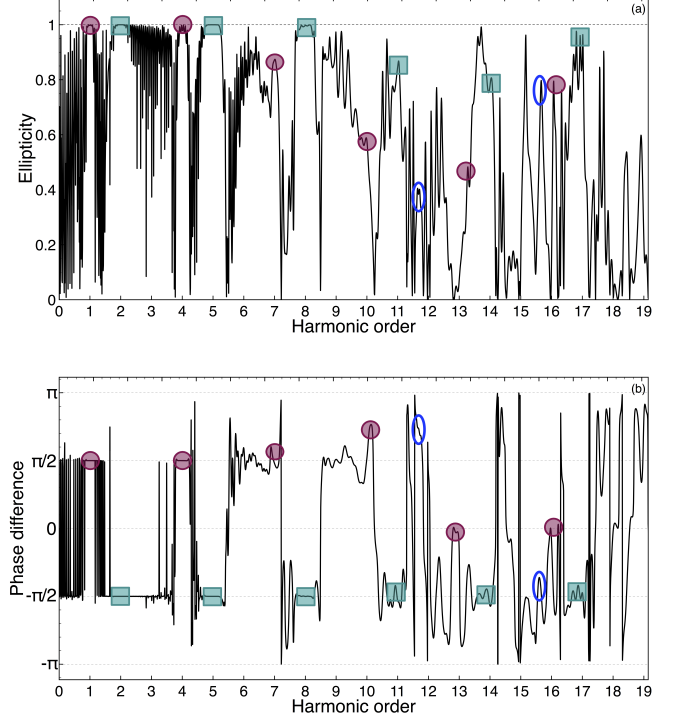
(maroon circles), and their ellipticity is closer to unity than that of the right subpeaks (teal squares), as seen in Fig. 7. In the cutoff region, H67–74, both left and right subpeaks exhibit again almost perfect circular polarization. The transformations of the polarization properties of the above-threshold harmonics with their order could reflect the shifts of their emission times within the same optical cycle. With increasing harmonic order, the emission time of the harmonic is shifted backwards, as seen in the time-frequency spectrum, Fig. 4. Detailed analysis of this phenomenon could be a subject of a separate study.

VII. CONCLUSION

In this paper, we have presented a detailed investigation and analysis of H_2^+ diatomic molecules subject to bichromatic (ω, 2ω) tailored counter-rotating circularly polarized intense laser fields. The intensities used in the calculations have been tailored through the use of classical trajectory analysis to produce three returns per T_2 optical cycle. The generated high-order harmonics exhibit circular polarization up to harmonic orders of H81. The
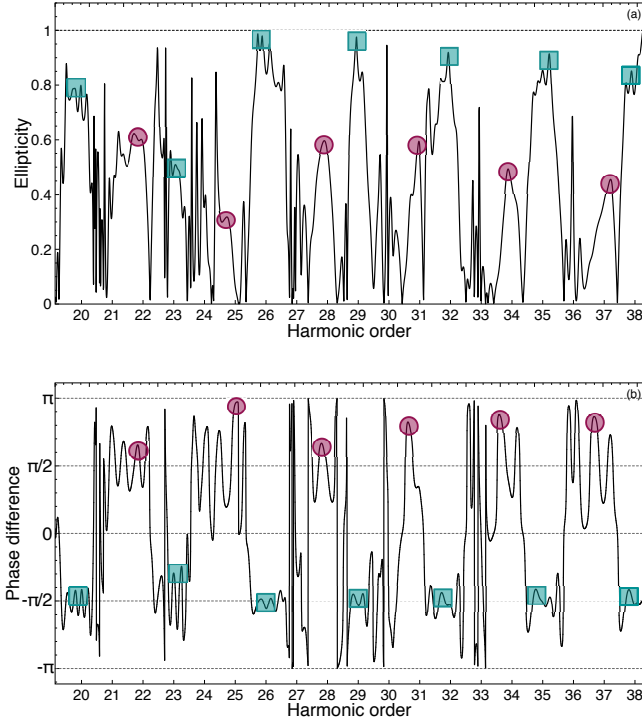
FIG. 6. (Color online) (a) Ellipticity and (b) phaseshift between the x and y components of the harmonic field (above-threshold harmonics; plateau region) from H_2^+ as a function of harmonic order. The laser parameters used are the same as those in Fig. 3. The filled maroon circles and filled teal squares mark the harmonic peak positions within each doublet.

HHG spectrum has a doublet structure where the harmonics within the same doublet have opposite (left and right) circular polarizations. The quantum SST analysis of the dipole accelerations shows distinctly three returns per T_2 optical cycle, agreeing with the proposed controlled classical trajectories analysis. In particular, we reveal that electron recollisions in molecular systems can be controlled through tailored bichromatic counter-rotating circularly polarized intense laser fields.

Furthermore, we find that excited-state resonances in the HHG spectrum can have effects on neighboring harmonics causing the phase and ellipticity to be altered from perfect circular polarization. Our study provides informative findings on the delicate electron dynamics in the below-, near-, and above-threshold harmonic regimes for diatomic molecules. Our findings can also be extended to facilitate the user-defined control of the elec-tron quantum paths for experimental implementation of ultrashort and intense coherent light sources and frequency comb source, both in the VUV and soft-x-ray regime, in the future.
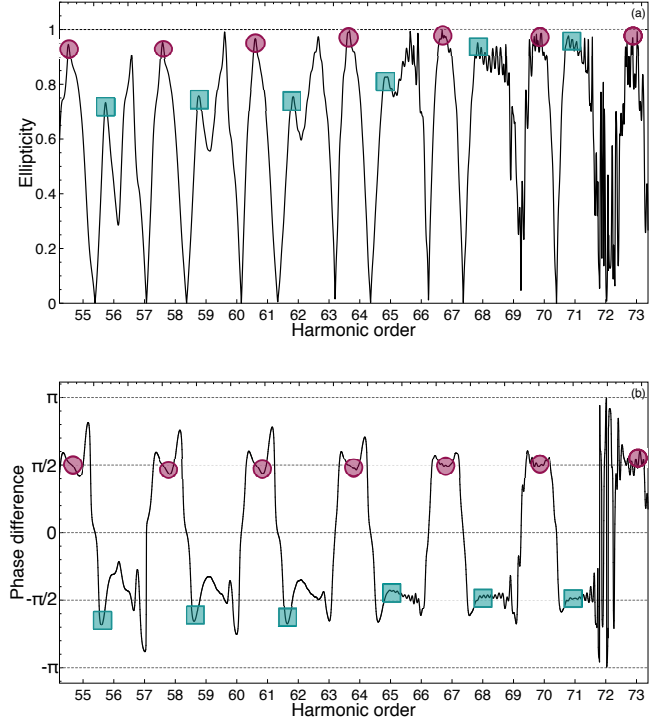

FIG. 7. (Color online) (a) Ellipticity and (b) phaseshift between the x and y components of the harmonic field (above-threshold harmonics; cutoff region) from H_2^+ as a function of harmonic order. The laser parameters used are the same as those in Fig. 3. The filled maroon circles and filled teal squares mark the harmonic peak positions within each doublet.

[1] T. Fan, P. Grychtol, R. Knut, C. Hernndez-Garca, D. D. Hickstein, D. Zusin, C. Gentry, F. J. Dollar, C. A. Mancuso, C. W. Hogle, et al., Proc. Natl. Acad. Sci. U.S.A. **112**, 14206 (2015).

[2] M. Chini, X. Wang, Y. Cheng, H. Wang, Y. Wu, E. Cunningham, P.-C. Li, J. Heslar, D. Telnov, S. Chu, et al., Nat. Photonics **8**, 437 (2014).

[3] I.-Y. Park, S. Kim, J. Choi, D.-H. Lee, Y.-J. Kim,

M. Kling, M. Stockman, and S.-W. Kim, Nat. Photonics **5**, 677 (2011).

[4] S. Kim, J. Jin, Y.-J. Kim, I.-Y. Park, K. Seung-Woo, and S.-W. Kim, Nature **453**, 757 (2008).

[5] J. Heslar, D. A. Telnov, and S. I. Chu, Phys. Rev. A **93**, 063401 (2016).

[6] A. Rundquist, C. G. Durfee, Z. Chang, C. Herne, S. Backus, M. M. Murnane, and H. C. Kapteyn, Science **280**, 1412 (1998).

[7] A. Fleischer, O. Kfir, T. Diskin, P. Sidorenko, and O. Cohen, Nat. Photonics **8**, 543 (2014).

[8] O. Kfir, P. Grychtol, E. Turgut, R. Knut, D. Zusin, A. Fleischer, E. Bordo, T. Fan, D. Popmintchev, T. Popmintchev, et al., J. Phys. B **49**, 123501 (2016).

[9] E. Turgut, C. La-o vorakiat, J. M. Shaw, P. Grychtol, H. T. Nembach, D. Rudolf, R. Adam, M. Aeschlimann, C. M. Schneider, T. J. Silva, et al., Phys. Rev. Lett. **110**, 197201 (2013).

[10] S. Mathias, C. La-O-Vorakiat, P. Grychtol, P. Granitzka, E. Turgut, J. M. Shaw, R. Adam, H. T. Nembach, M. E. Siemens, S. Eich, et al., Proc. Natl. Acad. Sci. U.S.A. **109**, 4792 (2012).

[11] C. La-O-Vorakiat, M. Siemens, M. M. Murnane, H. C. Kapteyn, S. Mathias, M. Aeschlimann, P. Grychtol, R. Adam, C. M. Schneider, J. M. Shaw, et al., Phys. Rev. Lett. **103**, 257402 (2009).

[12] O. Kfir, P. Grychtol, E. Turgut, R. Knut, D. Zusin, D. Popmintchev, T. Popmintchev, H. Nembach, J. M. Shaw, A. Fleischer, et al., Nat. Photonics **9**, 99 (2015).

[13] D. B. Milosevic, J. Phys. B **48**, 171001 (2015).

[14] S. Long, W. Becker, and J. K. McIver, Phys. Rev. A **52**, 2262 (1995).

[15] H. Eichmann, A. Egbert, S. Nolte, C. Momma, B. Wellegehausen, W. Becker, S. Long, and J. K. McIver, Phys. Rev. A **51**, R3414 (1995).

[16] K. M. Dorney, J. L. Ellis, C. Hernández-García, D. D. Hickstein, C. A. Mancuso, N. Brooks, T. Fan, G. Fan, D. Zusin, C. Gentry, et al., Phys. Rev. Lett. **119**, 063201 (2017).

[17] J. Heslar, D. A. Telnov, and S. I. Chu, Phys. Rev. A **96**, 063404 (2017).

[18] M. Abramowitz and I. Stegun, eds., *Handbook of Mathematical Functions* (Dover, New York, 1965).

[19] D. A. Telnov and S. I. Chu, Phys. Rev. A **80**, 043412 (2009).

[20] D. A. Telnov, J. Heslar, and S. I. Chu, Phys. Rev. A **95**, 043425 (2017).

[21] J. Heslar and S. I. Chu, Sci. Rep. **6**, 37774 (2016).

[22] K. N. Avanaki, D. A. Telnov, and S. I. Chu, J. Phys. B **49**, 114002 (2016).

[23] S. K. Son, D. A. Telnov, and S. I. Chu, Phys. Rev. A **82**, 043829 (2010).

[24] D. A. Telnov and S. I. Chu, Phys. Rev. A **76**, 043412 (2007).

[25] X. M. Tong and S. I. Chu, Chem. Phys. **217**, 119 (1997).

[26] E. Pisanty, S. Sukiasyan, and M. Ivanov, Phys. Rev. A **90**, 043829 (2014).

[27] Y. L. Sheu, L. Y. Hsu, H. T. Wu, P. C. Li, and S. I. Chu, AIP Adv. **4**, 117138 (2014).

[28] P. Flandrin, *Time-frequency/time-scale Analysis* (Academic Press, 1999).

[29] P. C. Li, Y. L. Sheu, C. Laughlin, and S. I. Chu, Phys. Rev. A **90**, 041401(R) (2014).

[30] P. C. Li, Y. L. Sheu, C. Laughlin, and S. I. Chu, Nat. Commun. **6**, 8178 (2015).

[31] Y. C. Chen, M. Y. Cheng, and H. T. Wu, J. R. Stat. Soc. Ser. B Stat. Methodol. **76**, 651 (2014).

[32] Y. F. Suprunenko, P. T. Clemson, and A. Stefanovska, Phys. Rev. Lett. **111**, 024101 (2013).

[33] H. T. Wu, Y. H. Chan, Y. T. Lin, and Y. H. Yeh, Appl. Comput. Harmon. Anal. **36**, 354 (2014).

[34] J. Heslar and S. I. Chu, Phys. Rev. A **95**, 043414 (2017).